IMA Journal of Applied Mathematics (2019) **84**, 605–631
doi:10.1093/imamat/hxz006
Advance Access publication on 18 March 2019

Analysis of a fractal ultrasonic transducer with a range of piezoelectric length scales

Ebrahem A. Algehyne and Anthony J. Mulholland*
Department of Mathematics and Statistics, University of Strathclyde, 26 Richmond Street, Glasgow G1 1XH, UK
*Corresponding author: anthony.mulholland@strath.ac.uk

[Received on 19 December 2017; revised on 19 October 2018; accepted on 16 February 2019]

The transmission and reception sensitivities of most piezoelectric ultrasonic transducers are enhanced by their geometrical structures. This structure is normally a regular, periodic one with one principal length scale, which, due to the resonant nature of the devices, determines the central operating frequency. There is engineering interest in building wide-bandwidth devices, and so it follows that, in their design, resonators that have a range of length scales should be used. This paper describes a mathematical model of a fractal ultrasound transducer whose piezoelectric components span a range of length scales. There have been many previous studies of wave propagation in the Sierpinski gasket but this paper is the first to study its complement. This is a critically important mathematical development as the complement is formed from a broad distribution of triangle sizes, whereas the Sierpinski gasket is formed from triangles of equal size. Within this structure, the electrical and mechanical fields fluctuate in tune with the time-dependent displacement of these substructures. A new set of basis functions is developed that allow us to express this displacement as part of a finite element methodology. A renormalization approach is then used to develop a recursion scheme that analytically describes the key components from the discrete matrices that arise. Expressions for the transducer's operational characteristics are then derived and analysed as a function of the driving frequency. It transpires that the fractal device has a significantly higher reception sensitivity (18 dB) and a significantly wider bandwidth (3 MHz) than an equivalent Euclidean (standard) device.

Keywords: fractal; ultrasound; transducer; finite element; renormalization; Sierpinski.

1. Introduction

Ultrasonic transducers are devices, which convert mechanical vibrations into electrical energy and conversely convert electrical energy into mechanical vibrations (Beyer & Letcher, 1969; Yang, 2006a,b). One of the main uses of ultrasonic transducers is the interrogation of optically opaque media, by emission of a mechanical wave (converted from electrical to mechanical energy) and the reception of the same wave (after navigating the medium of interest, the wave is converted back from mechanical to electrical energy). Piezoelectric ultrasonic transducers are the most common devices used to assess the structural integrity of safety critical components in, e.g. nuclear plants and are used extensively in medical imaging and therapies; there is therefore considerable interest in improving the design of these sensors and the global market for such devices is set to reach $6 billion by 2020 (iRAP, 2016). Piezoelectric ultrasonic transducers ordinarily use regular, periodic geometrical structures (Algehyne & Mulholland, 2015b; Alippi *et al.*, 1993; Hayward, 1984; Mulholland, 2008; Orr *et al.*, 2007).

Many biological species produce and receive ultrasound; however, generally speaking, their auditory physiology is highly complex in structure and often consists of resonators with a range of length scales (Algehyne & Mulholland, 2015a; Barlow *et al.*, 2016; Chiselev *et al.*, 2009; Eberl *et al.*, 2000; de Espinosa *et al.*, 2005; Miles & Hoy, 2006; Müller, 2004; Müller *et al.*, 2006; Nadrowski *et al.*, 2008; Robert & Göpfert, 2002). Due to this range of length scales, these natural transducers are able to operate over a wide range of frequencies (so-called broadband transducers). There is a strong motivation therefore to design a device whose structure spans a range of length scales. Fractal structures are a natural choice for such a device as they consist of a variety of length scales (Mulholland & Walker, 2011; Mulholland *et al.*, 2011; Orr *et al.*, 2008) and are therefore a prime candidate for investigation. Various authors have analysed wave propagation in fractal media (Abdulbake *et al.*, 2003, 2004; Barlow, 1998; Derfel *et al.*, 2012; Falconer & Hu, 2001; Giona, 1996; Giona *et al.*, 1996; Kigami, 2001; Strichartz, 1999) and in particular the Sierpinski gasket and its graph counterpart (Algehyne & Mulholland, 2015a, 2017). However, the Sierpinski gasket consists of a series of triangles that are all of the same size. To circumvent this disadvantage, this paper studies wave propagation in the complement of the Sierpinski gasket as this consists of triangles that span a broad range of length scales. This appears to be the first time wave propagation has been studied in this structure and opens up new possibilities for mathematicians who wish to study other types of field equations in a structure with multiple length scales. So this paper marks a significant departure from the previous works of Algehyne & Mulholland (2015a, 2017) as the introduction of piezoelectric resonators covering a broad range of length scales will produce a set of resonances across a range of frequencies and so provide the physical basis for a broadband device. This switch to the piezoelectric material being located in the complement of the Sierpinski gasket is the critical step in producing a marked improvement in the device performance. A new graph is derived here to describe this fractal and it transpires that it has the same adjacency matrix as its dual but now the edges are weighted. The physical model consists of the elastodynamic equations, Gauss's law for the electrical activity and a coupling of the electrical and mechanical waves through the piezoelectric constitutive equations. To describe this model on the fractal graph, a new set of finite element basis functions are derived whose support consists of the edges of the graph. The discrete equations that arise require the inversion of a large (in the case of a pre-fractal) or infinite-dimensional (for the fractal case) matrix in order to describe the dynamics of the device. Fortunately, the self-similar structure of the graph enables a renormalization approach to be utilized, which leads to a new set of nonlinear recursion relations. These recursion relations can be used to study the pre-fractal structures (for a finite number of iterations) or the fractal structure (by studying their steady states). This paper then compares the key operational characteristics of the pre-fractal ultrasound transducer with that of a standard transducer design. It transpires that the fractal device has a significantly higher reception sensitivity (18 dB) and a significantly wider bandwidth (3 MHz) than an equivalent Euclidean (standard) device (Hayward, 1984).

1.1 *The Sierpinski gasket dual*

This transducer starts off as a piezoelectric crystal in a triangular structure, connected to three half-sized copies of itself (see Fig. 1). The next generation ($n = 2$) connects three half-sized copies of the smaller triangles to each of these triangles. Continuing in this way, the complement (or dual) of the standard Sierpinski gasket is produced. Using the complement (the black triangles in Fig. 1) is vital as it has a range of triangle sizes, whereas the Sierpinski gasket is composed of triangles of the same size (the white triangles in Fig. 1) for a given fractal generation level.

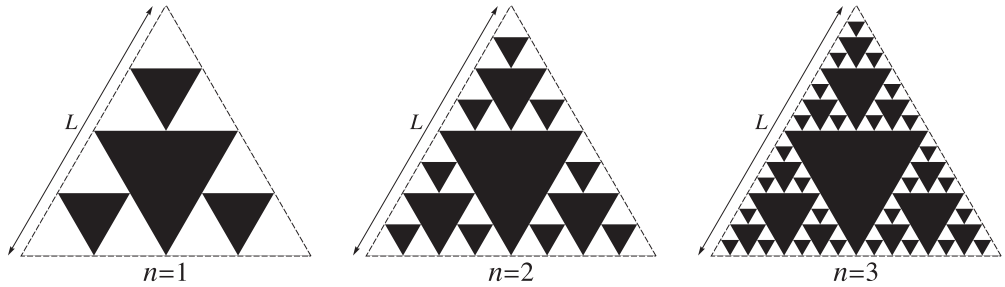

FIG. 1. The first few generations of the Sierpinski gasket (white triangles). The black triangles (the complement of the Sierpinski gasket) consist of piezoelectric material. The side length of the Sierpinski gasket is L for all generation levels.

1.2 *Problem statement*

Consider the vibrations of a Sierpinski gasket dual (denote this domain by Ω) made from a piezoelectric material (we will focus on PZT-5H) (Yang, 2006a) whose constitutive equations can be used to describe the interplay between the electrical and mechanical behaviour in Ω (Yang, 2006a,b)

$$T_{ij} = c_{ijkl}S_{kl} - e_{kij}E_k\,, \tag{1.1}$$

$$D_i = e_{ikl}S_{kl} + \varepsilon_{ik}E_k\,, \tag{1.2}$$

where the stress tensor is T_{ij}, the stiffness tensor is c_{ijkl}, the strain tensor is S_{kl}, the piezoelectric tensor is e_{kij}, the electric field vector is E_k, the electrical displacement tensor is D_i and the permittivity tensor is ε_{ik} (where the Einstein summation convention is adopted). The strain tensor describes the displacement gradients $u_{i,j}$ by $S_{ij} = (u_{i,j} + u_{j,i})/2$ and the electric field vector is related to the electric potential ϕ via $E_i = -\phi_{,i}$. Governing the piezoelectric material's dynamics is the following equation:

$$\rho_T \ddot{u}_i = T_{ji,j}, \tag{1.3}$$

subject to Gauss' law

$$D_{i,i} = 0, \tag{1.4}$$

where the density is ρ_T and the i^{th} component of displacement is u_i. At this point, we will consider the special case where there is only an out-of-plane displacement $\underline{u} = (0, 0, u_3(x_1, x_2, t))$ (this is the dominant direction of displacement in engineering applications). The piezoelectric material is polarized in the x_3 direction and the electrodes are arranged so that $\underline{E} = (E_1(x_1, x_2), E_2(x_1, x_2), 0)$. For the piezoelectric material, we choose PZT-5H (Auld, 1973). For this material (in Voigt notation), the various tensors above satisfy $c_{45} = c_{54} = 0$, $c_{44} = c_{55}$, $\varepsilon_{ik} = 0$ apart from $\varepsilon_{11} = \varepsilon_{22}$ and ε_{33}, and $e_{ikl} = 0$ apart from a small number of elements, which include $e_{113} = e_{131} = e_{223} = e_{232}$ (which in Voigt notation is e_{24}). Taking all of these restrictions on board then combining (1.1) with (1.3) gives

$$\rho_T \ddot{u}_3 = c_{44}(u_{3,11} + u_{3,22}) - e_{24}(E_{1,1} + E_{2,2}). \tag{1.5}$$

Combining (1.2) and (1.4) gives

$$E_{1,1} + E_{2,2} = -\frac{e_{24}}{\varepsilon_{11}}(u_{3,11} + u_{3,22}). \tag{1.6}$$

Combining (1.5) and (1.6) then gives

$$\ddot{u}_3 = c_T^2 \nabla^2 u_3, \tag{1.7}$$

where $\nabla^2 = \partial^2/\partial x_1^2 + \partial^2/\partial x_2^2$, $c_T = \sqrt{c_{44}^T/\rho_T}$ is the shear wave velocity and $c_{44}^T = c_{44} + e_{24}^2/\varepsilon_{11}$ is the piezoelectrically stiffened shear modulus. We apply the boundary conditions of continuity of force and displacement on $\partial\Omega$ as well as the initial conditions $u_3(\underline{x}, 0) = \dot{u}_3(\underline{x}, 0) = 0$. The challenge is to solve the above equations to calculate the dynamics of this device and to then use that to assess its performance as an ultrasonic transducer.

1.3 *Galerkin discretization*

Non-dimensionalizing via $\theta = c_T t/h^{(n)}$ and using the Laplace transform $\mathscr{L} : \theta \to q$ then gives (dropping the subscript on u)

$$q^2\, \bar{u} = \left(h^{(n)}\right)^2 \nabla^2 \bar{u}. \tag{1.8}$$

We will seek a weak solution $\bar{u} \in H^1(\Omega)$ where on the boundary $\bar{u} = \bar{u}_{\partial\Omega} \in H^1(\partial\Omega)$. We multiply by a test function $w \in H_B^1(\Omega)$, where $H_B^1(\Omega) := \left\{w \in H^1(\Omega) : w = 0 \text{ on } \partial\Omega\right\}$, integrate over the region Ω and use Green's first identity $\int_\Omega \psi\ \nabla^2\phi\, dv = \oint_{\partial\Omega} \psi(\nabla\phi\,.\,\underline{n})\, dr - \int_\Omega \nabla\phi\,.\,\nabla\psi\, dv$, where $\underline{n}$ is the outward pointing unit normal of surface element dr. So, we seek $\bar{u} \in H^1(\Omega)$ such that

$$q^2 \int_\Omega \bar{u}\, w\, \mathrm{d}\underline{x} = -\left(h^{(n)}\right)^2 \int_\Omega \nabla\bar{u}\,.\,\nabla w\, \mathrm{d}\underline{x},$$

where $w \in H_B^1(\Omega)$. Following a standard Galerkin approach, we employ the finite-dimensional subspaces S_S and $S_B = S_S \cap H_B^1(\Omega)$ rather than $H^1(\Omega)$ and $H_B^1(\Omega)$ and $U_B \in S_S$ to approximate $\bar{u}_{\partial\Omega}$ on the boundary $\partial\Omega$. The resulting discrete problem then requires $\bar{U} \in S_S$ to be found where

$$q^2 \int_\Omega \bar{U}\, \phi_j\, \mathrm{d}\underline{x} = -\left(h^{(n)}\right)^2 \int_\Omega \nabla\bar{U}\,.\,\nabla\phi_j\, \mathrm{d}\underline{x}, \quad j = 1, \ldots, N_n, \tag{1.9}$$

where $\{\phi_1, \phi_2, \ldots, \phi_{N_n}\}$ forms a basis of S_B. The dynamics of each triangular component in Ω will be described here by the dynamics of a single point at the centre of each of these components. Each of the basis functions will be centred on each of these points. Each triangular component in Ω is connected to some adjacent components and this connectivity will be captured here by joining these adjacent single points (or vertices) via edges to form a graph. The Sierpinski gasket graph of degree 3, SG, is the graph equivalent of the Sierpinski gasket (Schwalm & Schwalm, 1988). The dual graph $\left(\overline{\mathrm{SG}}\right)$ is introduced in this paper and is constructed by a process that starts from the order $n = 1$ design (which consists of four piezoelectric triangles) and assigns a vertex to the centre of each of the smaller triangles and, by connecting these vertices together with edges whose length is the side length of the larger triangle, the $\overline{\mathrm{SG}}$ weighted graph at generation level $n = 1$ is constructed (see Fig. 2).

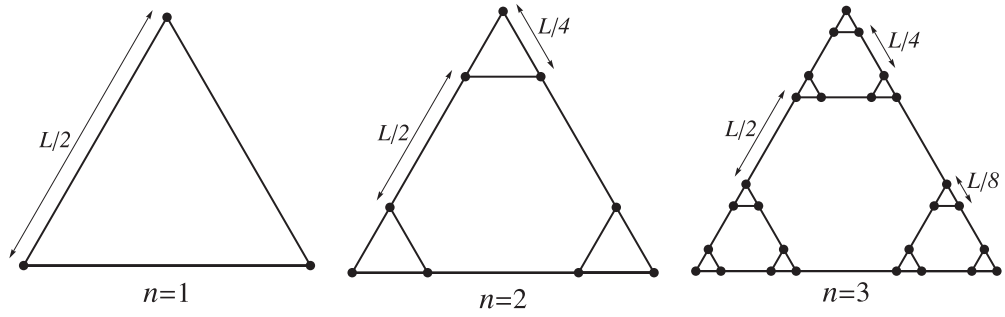

FIG. 2. The first few generations of the weighted Sierpinski gasket graph $\overline{\mathrm{SG}}$.

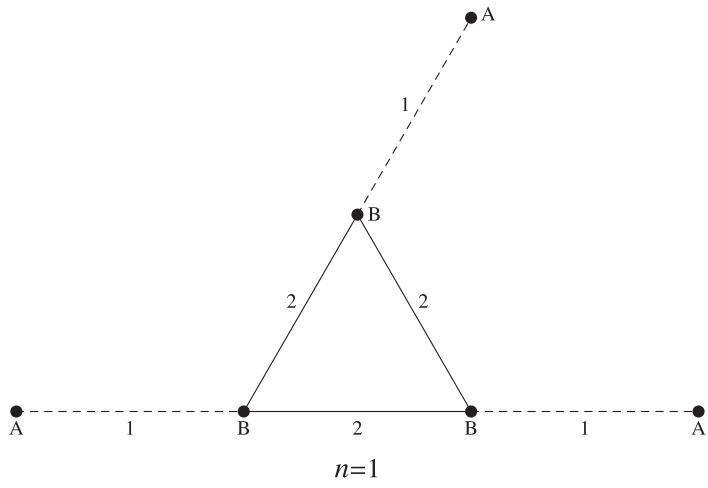

FIG. 3. The Sierpinski gasket dual lattice $\overline{\mathrm{SG}}(3)$ at generation level $n = 1$. Vertices $B \in V_{\Omega_n^o}$ or $V_{\partial\Omega_n^o}$ in this level $n = 1$ are the input/output vertices, and vertices $A \in V_{\partial\Omega_n}$ are fictitious vertices used to accommodate the boundary conditions.

The Sierpinski gasket has side length L units, which remain constant as the generation level n increases. The length of the smallest edge in the weighted graph $\overline{\mathrm{SG}}^{(n)}$ is $h^{(n)} = L/2^n$ and the longest edge length that connects the three $\overline{\mathrm{SG}}^{(n-1)}$ graphs is $h^{(1)} = L/2$. Then the overall diameter of the graph $L_{\mathrm{SG}}^{(n)} = nL/2$ and the total number of vertices is $N_n = 3^n$. The vertex degree is 3 apart from the boundary vertices (input/output vertices), which have degree 2 and $M_n = 3(3^n - 1)/2$ denotes the total number of edges at generation level n. The boundary vertices are used to interact with external loads (both electrical and mechanical) and fictitious vertices are introduced to cope with these interfacial boundary conditions. Denote by Ω_n the set of points lying on the edges or vertices of the weighted graph $\overline{\mathrm{SG}}^{(n)}$ and denote the region's boundary by $\partial\Omega_n$.

DEFINITION 1.1 Denote the set of vertices in Ω_n as V_{Ω_n}, the set of fictitious vertices as $V_{\partial\Omega_n}$ (these are vertices $N_n + 1, N_n + 2$ and $N_n + 3$), the set of interior vertices as $V_{\Omega_n^o}$ (so $V_{\Omega_n^o} = V_{\Omega_n} \setminus V_{\partial\Omega_n}$) and the set of input/output vertices as $V_{\partial\Omega_n^o}$ (these are vertices $1, m_n = (N_n + 1)/2$ and N_n) (see Figs 3 and 4). E_{Ω_n} is the set of edges in Ω_n, the set of edges joining vertices in $V_{\partial\Omega_n^o}$ to vertices in $V_{\partial\Omega_n}$ is

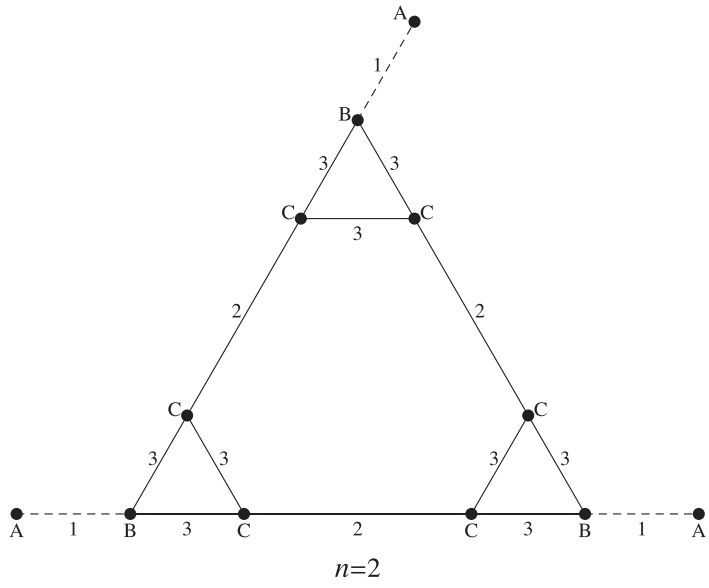

FIG. 4. The Sierpinski gasket dual lattice $\overline{\mathrm{SG}}(3)$ at generation level $n = 2$. Vertices B and $C \in V_{\Omega_n^o}$ and vertices $B \in V_{\partial\Omega_n^o}$. Vertices $A \in V_{\partial\Omega_n}$ are fictitious vertices used to accommodate the boundary conditions.

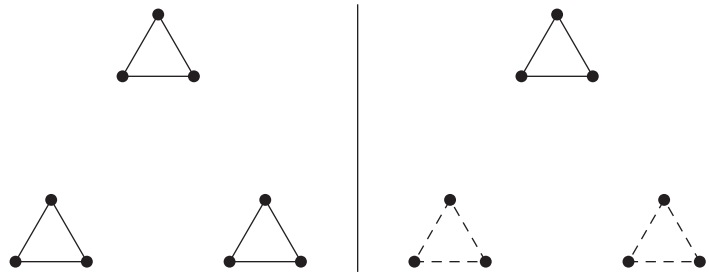

FIG. 5. Illustration of the identity $E^{(p)}_{\Omega_n^o} = \bar{E}^{(p-1)}_{\Omega_{n-1}^o}$.

denoted by $E_{\partial\Omega_n}$ and $E_{\Omega_n^o}$ is the set of the interior edges ($E_{\Omega_n^o} = E_{\Omega_n} \setminus E_{\partial\Omega_n}$). Denote by $E^{(p)}_{\Omega_n^o}$ the set of edges in $E_{\Omega_n^o}$ of length $h^{(p)}$ and by $\bar{E}^{(p)}_{\Omega_n^o}$ three copies of $E^{(p)}_{\Omega_n^o}$ (the adjacency matrix for $\bar{E}_{\Omega_n^o}$ is a block diagonal matrix where each block is the adjacency matrix for $E_{\Omega_n^o}$). $E^{(p)}_{\Omega_n}$ and $\bar{E}^{(p)}_{\Omega_n}$ are defined similarly using the complete set of edges in Ω_n. Also, $\bar{E}_{\partial\Omega_n}$ is three copies of the boundary edges $E_{\partial\Omega_n}$. Hence, $\bar{E}^{(p-1)}_{\Omega_{n-1}} = E^{(p)}_{\Omega_n}$ if $p < n$, $\bar{E}^{(p-1)}_{\Omega_{n-1}^o} = E^{(p)}_{\Omega_n^o}$ for $p \leqslant n$ (Fig. 5 graphically illustrates this identity) and $E^{(p)}_{\Omega_n^o} = E^{(p)}_{\Omega_n}$ if $p < n$.

Let ϕ_i, $i \in V_{\Omega_n}$ form a set of basis functions for the vertex displacements and let

$$\bar{U} = \sum_{i=1}^{N_n} U_i \phi_i + \sum_{i \in V_{\partial\Omega_n}} U_{B_i} \phi_i. \tag{1.10}$$

Hence, (1.9) becomes

$$A_{ji}^{(n)} U_i = b_j^{(n)}, \tag{1.11}$$

where

$$A_{ji}^{(n)} = q^2 H_{ji}^{(n)} + \left(h^{(n)}\right)^2 K_{ji}^{(n)}, \tag{1.12}$$

$$H_{ji}^{(n)} = \int_{\Omega_n} \left(\phi_j \phi_i\right) \mathrm{d}\underline{x}, \tag{1.13}$$

$$K_{ji}^{(n)} = \int_{\Omega_n} \left(\nabla \phi_j \,.\, \nabla \phi_i\right) \mathrm{d}\underline{x} \tag{1.14}$$

and

$$b_j^{(n)} = -\sum_{i \in V_{\partial\Omega_n}} \left(\int_{\partial\Omega_n} \left(q^2 \phi_j \phi_i + \left(h^{(n)}\right)^2 \nabla \phi_j \,.\, \nabla \phi_i \right) \mathrm{d}\underline{x} \right) U_{B_i}, \quad j \in V_{\partial\Omega_n^o}. \tag{1.15}$$

LEMMA 1.1 The basis function ϕ_j for vertex j in the element (the edge) joining vertices j and k at fractal generation level n is given by

$$\begin{aligned}
&\phi_j\left(x, y, x_j, y_j, x_k, y_k, x_m, y_m, x_l, y_l\right) \\
&\quad = \left((y - y_k)(x_m + x_l) - (x - x_k)(y_m + y_l) + 2(x y_k - x_k y) + x_j y - x_j y_k - x y_j + x_k y_j + x y_k - x_k y\right) \Big/ \\
&\qquad \left((y_j - y_k)(x_m + x_l) - (x_j - x_k)(y_m + y_l) + 2(x_j y_k - x_k y_j)\right),
\end{aligned} \tag{1.16}$$

where, for edges of length greater than $h^{(n)}$ and $n \geqslant 2$, the two other adjacent vertices to vertex j are l and m. For interior edges of length $h^{(n)}$ and $n \geqslant 1$, then vertex l is equal to vertex j and vertex m is the vertex that is connected to vertex j by the other edge of length $h^{(n)}$. For exterior edges—these will have length $h^{(n)}$—then vertices l and m are also the two interior vertices adjacent to vertex j. Hence,

$$\begin{aligned}
&\nabla \phi_j(x, y, x_j, y_j, x_k, y_k, x_m, y_m, x_l, y_l) \\
&\quad = \left(\frac{-(y_j + y_m + y_l) + 3y_k}{(y_j - y_k)(x_m + x_l) - (x_j - x_k)(y_m + y_l) + 2(x_j y_k - x_k y_j)}, \right. \\
&\qquad \left. \frac{x_j + x_m + x_l - 3x_k}{(y_j - y_k)(x_m + x_l) - (x_j - x_k)(y_m + y_l) + 2(x_j y_k - x_k y_j)} \right).
\end{aligned} \tag{1.17}$$

Proof. The basis function is chosen to be linear having a value of one at vertex j and a value of zero at vertex k. So $\phi_j^{(n)}$ is a straight line lying in a plane S_P containing the points $P_2 = (x_k, y_k, 0)$ and $P_1 = (x_j, y_j, 1)$. To make this plane unique, a third point is required. When edge jk is longer than $h^{(n)}$,

then, to retain the symmetry inherent to the $\overline{\mathrm{SG}}$ graph, this third point is chosen as the centroid of the triangle formed by the two other vertices ($\underline{x}_m$ and $\underline{x}_l$) connected to vertex j and vertex j itself. When an interior edge jk has length $h^{(n)}$, then this third point is chosen as the centroid of the triangle formed by the two interior vertices that are connected to vertex j by edges of length $h^{(n)}$. So let P_3 be the point $(x_j + x_m + x_l, y_j + y_m + y_l, 0)/3$. The vectors $\underline{a} = \overrightarrow{OP_1} - \overrightarrow{OP_3}$ and $\underline{b} = \overrightarrow{OP_2} - \overrightarrow{OP_3}$ lie in this plane and so the equation of the plane is $(\underline{a} \times \underline{b}) \cdot \underline{x} = (\underline{a} \times \underline{b}) \cdot \overrightarrow{OP_1}$. This is a scalar equation with the unknowns being the components of the vector $\underline{x} = (x, y, z)$. This equation is manipulated to make z the subject of the equation and the basis function in (1.16) is then given by the right-hand side of this equation. The gradient then follows. □

For a particular element of length $h^{(p)}$ lying between vertex j and vertex k, the isoparametric representation, given by

$$(x(s), y(s)) = \left((x_k - x_j)s + x_j, (y_k - y_j)s + y_j\right) \tag{1.18}$$

is employed, where $s \in [0, 1]$ and $\left|d\underline{x}\right| = h^{(p)}\, ds$.

2. Derivation of the matrix recursions

Using the basis function derived in Lemma 1.1, it can be shown that the matrix H at fractal generation level n can be related to its counterpart at level $n - 1$.

LEMMA 2.1

$$\hat{H}_{ji}^{(n)} = \bar{\hat{H}}_{ji}^{(n-1)} + \Upsilon^{(n)} W_{ji}^{(n)} + \vartheta^{(n)} P_{ji}^{(n)}, \quad j, i \in V_{\Omega_n^o}, \tag{2.1}$$

where $\bar{H}_{ji}^{(n-1)}$ is a block diagonal matrix consisting of three blocks of matrix $H_{ji}^{(n-1)}$ for $n \geqslant 2$, $\bar{\hat{H}}_{ji}^{(n-1)} = \bar{H}_{ji}^{(n-1)}/h^{(n)}$, $\hat{H}_{ji}^{(n)} = H_{ji}^{(n)}/h^{(n)}$, $\Upsilon^{(n)} = (2^{n-1} - 1)/3$, $\vartheta^{(n)} = 2^{n-1}/6$, $W_{ji}^{(n)} = \mathbb{1}_{V_{\Omega_n}^{(1)}}(j)\mathbb{1}_{\{0\}}(i - j)$ (where $\mathbb{1}_{\{A\}}(a)$ is the indicator function, which equals 1 if $a \in A$ and 0 otherwise) and $P_{ji}^{(n)} = \mathbb{1}_{E_{\Omega_n}^{(1)}}(ji)$.

Proof. By using (1.13) and (1.18) for edge jk of length $h^{(p)}$, then

$${}^{jk}H_{cd}^{(n,p)} = \int_{jk \in E_{\Omega_n}} \phi_c\, \phi_d\, \mathrm{d}\underline{x} = 2^{n-p} h^{(n)} \int_0^1 \phi_c\left(x(s), y(s)\right)\, \phi_d\left(x(s), y(s)\right)\, \mathrm{d}s. \tag{2.2}$$

From (1.16), the basis function at vertex j (which has coordinates (a, b)) along a typical edge $jk \in E_{\Omega_n}^{(p)}$ where $p < n$ is

$$\phi_j(x, y) = \frac{1}{h^{(n)}} \left((a - x)(3 + 2^{(1+p-n)}) - (b - y)\sqrt{3} + h^{(n)}\right) \tag{2.3}$$

and at vertex k (which has coordinates $(a + 2^{(n-p-1)}h^{(n)}, b + 2^{(n-p-1)}\sqrt{3}h^{(n)})$) is

$$\phi_k(x, y) = \frac{1}{h^{(n)}} \left((a - x)(3 + 2^{p-n}) - \sqrt{3}(b - y)\left(1 + 2^{p-n}\right)\right). \tag{2.4}$$

Substituting (1.18) into (2.3) and (2.4) gives

$$\phi_j\,(x(s), y(s)) = 1 - s$$

and

$$\phi_k\,(x(s), y(s)) = s.$$

Now if $(c = d = j)$ or $(c = d = k)$ in (2.2), then

$${}^{jk}H_{jj}^{(n,p)} = 2^{n-p}h^{(n)} \int_0^1 (1-s)^2\ \mathrm{d}s = \frac{2^{n-p}}{3}h^{(n)} = {}^{jk}H_{kk}^{(n,p)}$$

and if ($c = j$ and $d = k$) or ($c = k$ and $d = j$) in (2.2), then

$${}^{jk}H_{jk}^{(n,p)} = 2^{n-p}h^{(n)} \int_0^1 (1-s)\,s\,\mathrm{d}s = \frac{2^{n-p}}{6}h^{(n)} = {}^{jk}H_{kj}^{(n,p)}.$$

A similar calculation can be conducted for the case $p = n$ albeit the basis function calculation is slightly different and follows the prescription in the proof of Lemma 2. So (2.2) becomes, for $jk \in E_{\Omega_n}^{(p)}$, $n \geqslant 1$ and $p \leqslant n$

$${}^{jk}H_{cd}^{(n,p)} = 2^{n-p}h^{(n)} \begin{cases} \frac{1}{3} & \text{if } (c = d = j) \text{ or } (c = d = k) \\ \frac{1}{6} & \text{if } (c = j \text{ and } d = k) \text{ or } (c = k \text{ and } d = j),\ j \neq k \\ 0 & \text{otherwise.} \end{cases} \tag{2.5}$$

We now consider the basis functions at input/output vertices $V_{\partial\Omega_n^o}$ and the integration of (2.2) in the boundary edges $jk \in E_{\partial\Omega_n}$. Equation (2.2) becomes

$${}^{jk}H_{cd}^{(n,n)} = h^{(n)} \begin{cases} \frac{1}{3} & \text{if } (c = d = j \in V_{\partial\Omega_n^o}) \\ 0 & \text{otherwise.} \end{cases} \tag{2.6}$$

The matrix $H_{cd}^{(n)}$ is assembled element by element (edge by edge) as follows:

$$H_{cd}^{(n)} = \sum_{p=1}^{n} \sum_{jk \in E_{\Omega_n}^{(p)}} {}^{jk}H_{cd}^{(n,p)} = \sum_{p=2}^{n} \sum_{jk \in E_{\Omega_n}^{(p)}} {}^{jk}H_{cd}^{(n,p)} + \sum_{jk \in E_{\Omega_n}^{(1)}} {}^{jk}H_{cd}^{(n,1)}. \tag{2.7}$$

The first term on the right-hand side of this equation can be written as

$$\sum_{p=2}^{n}\sum_{jk\in E_{\Omega_n}^{(p)}} {}^{jk}H_{cd}^{(n,p)} = \sum_{p=2}^{n-1}\sum_{jk\in E_{\Omega_n}^{(p)}} {}^{jk}H_{cd}^{(n,p)} + \sum_{jk\in E_{\Omega_n}^{(n)}} {}^{jk}H_{cd}^{(n,n)}$$
$$= \sum_{p'=1}^{n-2}\sum_{jk\in E_{\Omega_n}^{(p'+1)}} {}^{jk}H_{cd}^{(n,p'+1)} + \sum_{jk\in E_{\Omega_n}^{(n)}} {}^{jk}H_{cd}^{(n,n)}.$$

Since $E_{\Omega_n^o}^{(p)} = \bar{E}_{\Omega_{n-1}^o}^{(p-1)}$, $E_{\Omega_n}^{(p)} = \bar{E}_{\Omega_{n-1}}^{(p-1)}$, and $E_{\partial\Omega_n} \subseteq \bar{E}_{\partial\Omega_{n-1}} \subseteq \bar{E}_{\Omega_{n-1}}^{(n-1)}$ for $1 < p < n$, then, $E_{\Omega_n}^{(n)} = E_{\Omega_n^o}^{(n)} \cup E_{\partial\Omega_n} = \bar{E}_{\Omega_{n-1}^o}^{(n-1)} \cup E_{\partial\Omega_n} = \left(\bar{E}_{\Omega_{n-1}}^{(n-1)} \setminus \bar{E}_{\partial\Omega_{n-1}}\right) \cup E_{\partial\Omega_n} = \bar{E}_{\Omega_{n-1}}^{(n-1)} \setminus \left(\bar{E}_{\partial\Omega_{n-1}} \setminus E_{\partial\Omega_n}\right)$. Hence,

$$\sum_{p=2}^{n}\sum_{jk\in E_{\Omega_n}^{(p)}} {}^{jk}H_{cd}^{(n,p)} = \sum_{p'=1}^{n-2}\sum_{jk\in \bar{E}_{\Omega_{n-1}}^{(p')}} {}^{jk}H_{cd}^{(n,p'+1)} + \sum_{jk\in \bar{E}_{\Omega_{n-1}}^{(n-1)}} {}^{jk}H_{cd}^{(n,n)} - \sum_{jk\in \bar{E}_{\partial\Omega_{n-1}}\setminus E_{\partial\Omega_n}} {}^{jk}H_{cd}^{(n,n)}$$
$$= \sum_{p'=1}^{n-1}\sum_{jk\in \bar{E}_{\Omega_{n-1}}^{(p')}} {}^{jk}H_{cd}^{(n,p'+1)} - \sum_{jk\in \bar{E}_{\partial\Omega_{n-1}}\setminus E_{\partial\Omega_n}} {}^{jk}H_{cd}^{(n,n)}.$$

It can be shown that ${}^{jk}H_{cd}^{(n,p'+1)} = {}^{jk}H_{cd}^{(n-1,p')}$, and then from (2.6),

$$\sum_{p=2}^{n}\sum_{jk\in E_{\Omega_n}^{(p)}} {}^{jk}H_{cd}^{(n,p)} = \bar{H}_{cd}^{(n-1)} - \frac{h^{(n)}}{3}W_{cd}^{(n)} \tag{2.8}$$

since in $\bar{E}_{\partial\Omega_{n-1}} \setminus E_{\partial\Omega_n}$ we have $c = d$ in (2.5), and $\bar{H}_{cd}^{(n-1)}$ is a block diagonal matrix of dimension $N_n \times N_n$ consisting of three blocks given by $H_{cd}^{(n-1)}$ of dimension $N_{n-1} \times N_{n-1}$. Now the second term on the right-hand side of (2.7) can be written as

$$\sum_{jk\in E_{\Omega_n}^{(1)}} {}^{jk}H_{cd}^{(n,1)} = 2^{n-1}h^{(n)}\left(\frac{1}{6}P_{cd}^{(n)} + \frac{1}{3}W_{cd}^{(n)}\right).$$

Combining this with (2.8), then (2.7) becomes

$$\hat{H}_{ji}^{(n)} = \bar{\hat{H}}_{ji}^{(n-1)} + \frac{1}{3}(2^{n-1}-1)W_{ji}^{(n)} + \frac{2^{n-1}}{6}P_{ji}^{(n)},$$

where $\bar{\hat{H}}_{ji}^{(n-1)} = \bar{H}_{ji}^{(n-1)}/h^{(n)}$ and $\hat{H}_{ji}^{(n)} = H_{ji}^{(n)}/h^{(n)}$. □

A similar approach can be used to derive the matrix $K_{ji}^{(n)}$.

LEMMA 2.2

$$\hat{K}_{ji}^{(n)} = \bar{\hat{K}}_{ji}^{(n-1)} + \epsilon^{(n)} W_{ji}^{(n)} + \chi^{(n)} P_{ji}^{(n)}, \quad j, i \in V_{\Omega_n^o}, \tag{2.9}$$

where $\bar{K}_{ji}^{(n-1)}$ is a block diagonal matrix consisting of three blocks of matrix $K_{ji}^{(n-1)}$ for $n \geqslant 2$, $\bar{\hat{K}}_{ji}^{(n-1)} = h^{(n)} \bar{K}_{ji}^{(n-1)}$, $\hat{K}_{ji}^{(n)} = h^{(n)} K_{ji}^{(n)}$, $\epsilon^{(n)} = 2^{n-1}(12 + 2^{4-2n} + 3(2^{3-n})) - 28$ and $\chi^{(n)} = 2^{n-1}(12 + 2^{3-2n} + 3(2^{3-n}))$.

Proof. By using (1.14) and (1.18) for edge jk of length $h^{(p)}$, then

$${}^{jk}K_{cd}^{(n,p)} = \int_{jk \in E_{\Omega_n}} \nabla \phi_c \,.\, \nabla \phi_d \, \mathrm{d}\underline{x} = 2^{n-p} h^{(n)} \int_0^1 \nabla \phi_c \,(x(s), y(s)) \,.\, \nabla \phi_d \,(x(s), y(s)) \, \mathrm{d}s. \tag{2.10}$$

Equations (2.3) and (2.4) give for $jk \in E_{\Omega_n}^{(p)}$ where $p < n$

$$\nabla \phi_j(x, y) = \frac{1}{h^{(n)}} \left(-\left(3 + 2^{(1-n+p)}\right), \sqrt{3} \right)$$

and

$$\nabla \phi_k(x, y) = \frac{1}{h^{(n)}} \left(-\left(3 + 2^{p-n}\right), \sqrt{3}\left(1 + 2^{p-n}\right) \right).$$

Now if $(c = d = j)$ or $(c = d = k)$ in (2.10), then

$$\begin{aligned} {}^{jk}K_{jj}^{(n,p)} &= 2^{n-p} h^{(n)} \int_0^1 \frac{1}{h^{(n)}} \left(-\left(3 + 2^{(1-n+p)}\right), \sqrt{3} \right) \cdot \frac{1}{h^{(n)}} \left(-\left(3 + 2^{(1-n+p)}\right), \sqrt{3} \right) \mathrm{d}s \\ &= \frac{2^{n-p}}{h^{(n)}} \left(12 + 2^{(2-2n+2p)} + 3\left(2^{(2-n+p)}\right) \right) = {}^{jk}K_{kk}^{(n,p)} \end{aligned}$$

and if $(c = j$ and $d = k)$ or $(c = k$ and $d = j)$ in (2.10), then

$$\begin{aligned} {}^{jk}K_{jk}^{(n,p)} &= 2^{n-p} h^{(n)} \int_0^1 \frac{1}{h^{(n)}} \left(-\left(3 + 2^{(1-n+p)}\right), \sqrt{3} \right) \cdot \frac{1}{h^{(n)}} \left(-\left(3 + 2^{p-n}\right), \sqrt{3}\left(1 + 2^{p-n}\right) \right) \mathrm{d}s \\ &= \frac{2^{n-p}}{h^{(n)}} \left(12 + 2^{(1-2n+2p)} + 3\left(2^{(2-n+p)}\right) \right) = {}^{jk}K_{kj}^{(n,p)}. \end{aligned}$$

Hence, for $jk \in E_{\Omega_n}^{(p)}$, $n \geqslant 2$ and $p < n$,

$${}^{jk}K_{cd}^{(n,p)} = \frac{2^{n-p}}{h^{(n)}} \begin{cases} 12 + 2^{(2-2n+2p)} + 3\left(2^{(2-n+p)}\right) & \text{if } (c = d = j) \text{ or } (c = d = k) \\ 12 + 2^{(1-2n+2p)} + 3\left(2^{(2-n+p)}\right) & \text{if } (c = j \text{ and } d = k) \text{ or } (c = k \text{ and } d = j) \\ 0 & \text{otherwise.} \end{cases} \tag{2.11}$$

A similar calculation can be undertaken for the case when $jk \in E^{(n)}_{\Omega^o_n}$ and $p = n$. It transpires that

$$ {}^{jk}K^{(n,n)}_{cd} = \frac{1}{h^{(n)}} \begin{cases} 4 & \text{if } (c = d = j) \text{ or } (c = d = k) \\ 2 & \text{if } (c = j \text{ and } d = k) \text{ or } (c = k \text{ and } d = j) \\ 0 & \text{otherwise.} \end{cases} \tag{2.12} $$

Similarly, for the boundary edges $jk \in E_{\partial\Omega_n}$, (2.10) becomes

$$ {}^{jk}K^{(n,n)}_{cd} = \frac{1}{h^{(n)}} \begin{cases} 28 & \text{if } (c = d = j \in V_{\partial\Omega^o_n}) \\ 0 & \text{otherwise.} \end{cases} \tag{2.13} $$

As before, the matrix $K^{(n)}_{cd}$ is assembled in an element by element (edge by edge) manner via

$$ K^{(n)}_{cd} = \sum_{p=1}^{n} \sum_{jk \in E^{(p)}_{\Omega_n}} {}^{jk}K^{(n,p)}_{cd} = \sum_{p=2}^{n} \sum_{jk \in E^{(p)}_{\Omega_n}} {}^{jk}K^{(n,p)}_{cd} + \sum_{jk \in E^{(1)}_{\Omega_n}} {}^{jk}K^{(n,1)}_{cd}. \tag{2.14} $$

The first term on the right-hand side of this equation can be written as

$$ \begin{aligned} \sum_{p=2}^{n} \sum_{jk \in E^{(p)}_{\Omega_n}} {}^{jk}K^{(n,p)}_{cd} &= \sum_{p=2}^{n-1} \sum_{jk \in E^{(p)}_{\Omega_n}} {}^{jk}K^{(n,p)}_{cd} + \sum_{jk \in E^{(n)}_{\Omega_n}} {}^{jk}K^{(n,n)}_{cd} \\ &= \sum_{p'=1}^{n-2} \sum_{jk \in E^{(p'+1)}_{\Omega_n}} {}^{jk}K^{(n,p'+1)}_{cd} + \sum_{jk \in E^{(n)}_{\Omega_n}} {}^{jk}K^{(n,n)}_{cd}. \end{aligned} $$

Since $E^{(p)}_{\Omega_n} = \bar{E}^{(p-1)}_{\Omega_{n-1}}$ for $1 < p < n$, and $E^{(n)}_{\Omega_n} = E^{(n)}_{\Omega^o_n} \cup E_{\partial\Omega_n} = \bar{E}^{(n-1)}_{\Omega^o_{n-1}} \cup E_{\partial\Omega_n} = \left(\bar{E}^{(n-1)}_{\Omega_{n-1}} \setminus \bar{E}_{\partial\Omega_{n-1}}\right) \cup E_{\partial\Omega_n} = \bar{E}^{(n-1)}_{\Omega_{n-1}} \setminus \left(\bar{E}_{\partial\Omega_{n-1}} \setminus E_{\partial\Omega_n}\right)$. Hence,

$$ \begin{aligned} \sum_{p=2}^{n} \sum_{jk \in E^{(p)}_{\Omega_n}} {}^{jk}K^{(n,p)}_{cd} &= \sum_{p'=1}^{n-2} \sum_{jk \in \bar{E}^{(p')}_{\Omega_{n-1}}} {}^{jk}K^{(n,p'+1)}_{cd} + \sum_{jk \in \bar{E}^{(n-1)}_{\Omega_{n-1}}} {}^{jk}K^{(n,n)}_{cd} - \sum_{jk \in \bar{E}_{\partial\Omega_{n-1}} \setminus E_{\partial\Omega_n}} {}^{jk}K^{(n,n)}_{cd} \\ &= \sum_{p'=1}^{n-1} \sum_{jk \in \bar{E}^{(p')}_{\Omega_{n-1}}} {}^{jk}K^{(n,p'+1)}_{cd} - \sum_{jk \in \bar{E}_{\partial\Omega_{n-1}} \setminus E_{\partial\Omega_n}} {}^{jk}K^{(n,n)}_{cd}. \end{aligned} $$

It can be shown that ${}^{jk}K_{cd}^{(n,p'+1)} = {}^{jk}K_{cd}^{(n-1,p')}$, and then from (2.13),

$$\sum_{p=2}^{n} \sum_{jk \in E_{\Omega_n}^{(p)}} {}^{jk}K_{cd}^{(n,p)} = \bar{K}_{cd}^{(n-1)} - \frac{28}{h^{(n)}} W_{cd}^{(n)} \tag{2.15}$$

by a similar argument to that in Lemma 2.1. Examining the second term on the right-hand side of (2.14), and using (2.11) with $p = 1$, gives

$$\begin{aligned} \sum_{jk \in E_{\Omega_n}^{(1)}} {}^{jk}K_{cd}^{(n,1)} &= \frac{2^{n-1}}{h^{(n)}} \left(12 + 2^{3-2n} + 3(2^{3-n})\right) P_{cd}^{(n)} \\ &\quad + \frac{2^{n-1}}{h^{(n)}} \left(12 + 2^{4-2n} + 3(2^{3-n})\right) W_{cd}^{(n)}. \end{aligned}$$

Combining this with (2.15), then (2.14) becomes

$$\hat{K}_{ji}^{(n)} = \bar{\hat{K}}_{ji}^{(n-1)} + \epsilon^{(n)} W_{ji}^{(n)} + \chi^{(n)} P_{ji}^{(n)},$$

where $\bar{\hat{K}}_{ji}^{(n-1)} = h^{(n)} \bar{K}_{ji}^{(n-1)}$, $\hat{K}_{ji}^{(n)} = h^{(n)} K_{ji}^{(n)}$, $\epsilon^{(n)} = 2^{n-1}(12 + 2^{4-2n} + 3(2^{3-n})) - 28$ and $\chi^{(n)} = 2^{n-1}(12 + 2^{3-2n} + 3(2^{3-n}))$. □

THEOREM 2.1

$$\hat{A}_{ji}^{(n)} = \bar{\hat{A}}_{ji}^{(n-1)} + \alpha^{(n)} W_{ji}^{(n)} + \beta^{(n)} P_{ji}^{(n)}, \tag{2.16}$$

where $\bar{A}_{ji}^{(n-1)}$ is a block diagonal matrix consisting of three blocks of matrix $A_{ji}^{(n-1)}$ for $n \geqslant 2$, $\bar{\hat{A}}_{ji}^{(n-1)} = \bar{A}_{ji}^{(n-1)}/h^{(n)}$, $\alpha^{(n)} = q^2 \Upsilon^{(n)} + \varepsilon^{(n)}$ and $\beta^{(n)} = q^2 \vartheta^{(n)} + \chi^{(n)}$.

Proof. Combining (2.1) and (2.9) gives (1.12) as

$$\begin{aligned} \hat{A}_{ji}^{(n)} &= q^2 \left(\bar{\hat{H}}_{ji}^{(n-1)} + \Upsilon^{(n)} W_{ji}^{(n)} + \vartheta^{(n)} P_{ji}^{(n)}\right) + \left(\bar{\hat{K}}_{ji}^{(n-1)} + \varepsilon^{(n)} W_{ji}^{(n)} + \chi^{(n)} P_{ji}^{(n)}\right) \\ &= q^2 \bar{\hat{H}}_{ji}^{(n-1)} + \bar{\hat{K}}_{ji}^{(n-1)} + \alpha^{(n)} W_{ji}^{(n)} + \beta^{(n)} P_{ji}^{(n)}. \end{aligned}$$

As discussed in Algehyne & Mulholland (2015a), when redimensionalizing, we need to rescale the frequency by $(c_T/h^{(n)})^{-1}$. Hence,

$$\hat{A}_{ji}^{(n)} = \bar{\hat{A}}_{ji}^{(n-1)} + \alpha^{(n)} W_{ji}^{(n)} + \beta^{(n)} P_{ji}^{(n)},$$

where $\bar{\hat{A}}_{ji}^{(n-1)} = q^2 \bar{\hat{H}}_{ji}^{(n-1)} + \bar{\hat{K}}_{ji}^{(n-1)}$. □

A similar treatment can be given to (1.15)

LEMMA 2.3

$$b_j^{(n)} = h^{(n)} \eta \, U_i \, \mathbb{1}_{E_{\partial\Omega_n}}(ji), \quad j \in V_{\partial\Omega_n^o}, \, i \in V_{\partial\Omega_n}, \tag{2.17}$$

where $\eta = 4 - q^2/6$.

Proof. By using (1.15) and (1.18) for edge ji, then

$$\begin{aligned} b_j^{(n)} &= -\sum_{i \in V_{\partial\Omega_n}} \left(\int_{ji \in E_{\partial\Omega_n}} \left(q^2 \phi_j \phi_i + \left(h^{(n)}\right)^2 \nabla\phi_j \,.\, \nabla\phi_i \right) d\underline{x} \right) U_{B_i} \\ &= -h^{(n)} \sum_{i \in V_{\partial\Omega_n}} \left(\int_0^1 \left(q^2 \phi_j \left(x(s), y(s)\right) \phi_i \left(x(s), y(s)\right) \right. \right. \\ &\quad \left. \left. + \left(h^{(n)}\right)^2 \nabla\phi_j \left(x(s), y(s)\right) \,.\, \nabla\phi_i \left(x(s), y(s)\right) \right) ds \right) U_{B_i}, \end{aligned} \tag{2.18}$$

where $j \in V_{\partial\Omega_n^o}$. From (1.16), the basis function at vertex $j \in V_{\partial\Omega_n^o}$ (without loss of generality, we will examine the vertex with coordinates $(a, 0)$) along a typical edge $ji \in E_{\partial\Omega_n}$ is

$$\phi_j(x, y) = \frac{1}{h^{(n)}} \left(a + h^{(n)} - x - 3\sqrt{3}y \right) \tag{2.19}$$

and at vertex $i \in V_{\partial\Omega_n}$ (which has coordinates $(a + h^{(n)}, 0)$) is

$$\phi_i(x, y) = \frac{1}{h^{(n)}} \left(-a + x + \frac{y}{\sqrt{3}} \right). \tag{2.20}$$

Substituting (1.18) into (2.19) and (2.20) gives

$$\phi_j \left(x(s), y(s)\right) = 1 - s \tag{2.21}$$

and

$$\phi_i \left(x(s), y(s)\right) = s. \tag{2.22}$$

In addition, (2.19) and (2.20) give

$$\nabla\phi_j \left(x(s), y(s)\right) = \frac{1}{h^{(n)}} \left(-1, -3\sqrt{3} \right) \tag{2.23}$$

and

$$\nabla\phi_i \left(x(s), y(s)\right) = \frac{1}{h^{(n)}} \left(1, +\frac{1}{\sqrt{3}} \right). \tag{2.24}$$

Substituting (2.21) to (2.24) into (2.18) gives

$$b_j^{(n)} = h^{(n)} \left(4 - \frac{q^2}{6}\right) U_i \quad j \in V_{\partial\Omega_n^o},\ i \in V_{\partial\Omega_n} \text{ and } ji \in E_{\partial\Omega_n}.$$

□

2.1 *Application of the mechanical boundary conditions*

The transducer is electrically coupled to a power supply and is immersed in a mechanical load and appropriate electrical and mechanical boundary conditions can be applied (Algehyne & Mulholland, 2015a).

THEOREM 2.2

$$U_i = G_{ji}^{(n)} \bar{\delta}_j, \tag{2.25}$$

where

$$G_{ji}^{(n)} = \left(\hat{A}_{ji}^{(n)} - \hat{B}_{ji}^{(n)}\right)^{-1} \tag{2.26}$$

represents the Green's transfer matrix, $\hat{B}_{ji}^{(n)} = \text{diag}\{\bar{\gamma}_1, \ldots, \bar{\gamma}_{m_n}, \ldots, \bar{\gamma}_{N_n}\}$, $\bar{\gamma}_j = \eta\gamma_j$, $\bar{\delta}_j = \eta\delta_j$,

$$\gamma_j = \begin{cases} \left(1 - qZ_B/Z_T\right)^{-1}, & j = 1 \\ \left(1 - qZ_L/Z_T\right)^{-1}, & j = m_n \text{ or } N_n \\ 0 & \text{otherwise,} \end{cases} \tag{2.27}$$

$$\delta_j = \begin{cases} -\gamma_1 \zeta Q / \left(c_{44}^T \xi\right), & j = 1 \\ \gamma_{m_n} \left(\zeta Q / \left(c_{44}^T \xi\right) - 2A_L qZ_L/Z_T\right), & j = m_n \text{ or } N_n \\ 0 & \text{otherwise,} \end{cases} \tag{2.28}$$

Z_B is the mechanical impedance of the backing material, $Z_L = \mu_L A_r / c_L$ is the mechanical impedance of the load, $Z_T = c_{44}^T A_r / c_T$, $\zeta = e_{24}/\varepsilon_{11}$, Q is the electrical charge, $\xi = A_r/h^{(n)}$, A_r is the cross-sectional area of the electrode, A_L is the amplitude of the incoming wave that is received by the transducer (in transmission mode A_L is zero), μ_L is the shear modulus of the load material and c_L is its wave speed.

Proof. From Algehyne & Mulholland (2017) $U_i = \gamma_j U_j + \delta_j$, $i \in V_{\partial\Omega_n}$, $j \in V_{\partial\Omega_n^o}$, $ji \in E_{\partial\Omega_n}$ and, hence, (2.17) becomes

$$b_j^{(n)} = h^{(n)} \bar{\gamma}_j U_j + h^{(n)} \bar{\delta}_j, \quad j \in V_{\partial\Omega_n^o}. \tag{2.29}$$

Putting this equation into (1.11) gives

$$\hat{A}_{ji}^{(n)} U_i = \bar{\gamma}_j U_j + \bar{\delta}_j.$$

Hence,

$$\left(\hat{A}_{ji}^{(n)} - \hat{B}_{ji}^{(n)}\right) U_i = \bar{\delta}_j.$$

□

3. Renormalization and the transducer operating characteristics

Using Theorem 2.2, a recursion relationship can be derived that relates the pivotal elements of the matrix $G_{ji}^{(n+1)}$ to those in $G_{ji}^{(n)}$.

LEMMA 3.1

$$\hat{G}^{(n+1)} = \bar{\hat{G}}^{(n)} - \bar{\hat{G}}^{(n)}\left(\alpha^{(n+1)} W^{(n+1)} + \beta^{(n+1)} P^{(n+1)}\right)\hat{G}^{(n+1)}, \tag{3.1}$$

where $\hat{G}^{(n)} = (\hat{A}^{(n)})^{-1}$ and $\bar{\hat{G}}^{(n)}$ is a block diagonal matrix consisting of three blocks of matrix $\hat{G}^{(n)}$.

Proof. From (2.25) and (2.27), it is clear that we only need to know the elements of $G_{ji}^{(n)}$ in columns $1, m_n$ and N_n. In addition, we will only require elements $U_j, j \in V_{\partial\Omega_n^o}$ and so we only need to be able to calculate the pivotal Green's functions $G_{ij}^{(n)}$, $i,j \in V_{\partial\Omega_n^o}$. If we temporarily ignore matrix $\hat{B}$ in (2.26) (associated with the application of the boundary conditions), then, due to the symmetries of the weighted $\overline{\text{SG}}$ graph, we have

$$\left(\hat{G}^{(n+1)}\right)^{-1} = \left(\bar{\hat{G}}^{(n)}\right)^{-1} + \alpha^{(n+1)} W^{(n+1)} + \beta^{(n+1)} P^{(n+1)}.$$

That is

$$\left(\bar{\hat{G}}^{(n)}\right)^{-1} = \left(\hat{G}^{(n+1)}\right)^{-1} - \left(\alpha^{(n+1)} W^{(n+1)} + \beta^{(n+1)} P^{(n+1)}\right).$$

Hence, using the $N_{n\times 1} \times N_{n\times 1}$ identity matrix denoted by I_{n+1},

$$\begin{aligned} I_{n+1} &= \bar{\hat{G}}^{(n)}\left(\left(\hat{G}^{(n+1)}\right)^{-1} - \left(\alpha^{(n+1)} W^{(n+1)} + \beta^{(n+1)} P^{(n+1)}\right)\right) \\ &= \bar{\hat{G}}^{(n)}\left(I_{n+1} - \left(\alpha^{(n+1)} W^{(n+1)} + \beta^{(n+1)} P^{(n+1)}\right)\hat{G}^{(n+1)}\right)\left(\hat{G}^{(n+1)}\right)^{-1}. \end{aligned}$$

Hence,

$$\hat{G}^{(n+1)} = \bar{\hat{G}}^{(n)} - \bar{\hat{G}}^{(n)}\left(\alpha^{(n+1)} W^{(n+1)} + \beta^{(n+1)} P^{(n+1)}\right)\hat{G}^{(n+1)}.$$

□

To calculate $G_{ji}^{(n)}$, the boundary conditions must be reintroduced and it can be shown that (Algehyne & Mulholland, 2017)

$$G^{(n)} = \hat{G}^{(n)} + \hat{G}^{(n)}\hat{B}^{(n)}G^{(n)}. \tag{3.2}$$

The renormalization recursion relationships for the pivotal Green's functions arise from the system of linear equations in $\hat{G}_{ji}^{(n+1)}$. The three subgraphs of Fig. 2 have a single connection point to one another at the corners and, due to the symmetries of the $\overline{\text{SG}}$ graph, the recursions in (3.1) give rise to only two pivotal Green's functions, known as, corner-to-same corner $\left(\hat{G}_{ii}^{(n)} = \hat{x}\right.$, say, where $\left.i \in V_{\partial\Omega_n^o}\right)$ and corner-to-other-corner $\left(\hat{G}_{jk}^{(n)} = \hat{y}\right.$, say, where $\left.j,k \in V_{\partial\Omega_n^o}, j \neq k\right)$; the so-called input/output vertices. For ease

of notation, let, $\hat{X} = \hat{G}_{ii}^{(n+1)}$ and $\hat{Y} = \hat{G}_{ij}^{(n+1)}$ where $i,j \in V_{\partial\Omega_n^o}$, $i \neq j$. The matrix is symmetrical and, consequently, $\hat{G}_{ij}^{(n)} = \hat{G}_{ji}^{(n)}$.

LEMMA 3.2 The renormalization recursion relations for the pivotal Green's functions (ignoring temporarily the boundary conditions) are given by

$$\hat{X} = \frac{3\left(\hat{x}-\hat{y}\right)\left(\hat{x}+2\hat{y}\right) + \Delta_1 + \Delta_2}{3\left(\hat{x}+\hat{y}\right)} \tag{3.3}$$

and

$$\hat{Y} = \frac{-\beta^{(n+1)}\hat{y}^2\left(1+(\hat{x}-\hat{y})(\alpha^{(n+1)}+\beta^{(n+1)})\right)}{\delta_1\delta_2}, \tag{3.4}$$

where $\Delta_1 = 2\hat{y}^2/\delta_1$, $\Delta_2 = 2\hat{y}^2(2+(\hat{x}-\hat{y})(2\alpha^{(n+1)}+\beta^{(n+1)}))/\delta_2$, $\delta_1 = 1+(\hat{x}+\hat{y})(\alpha^{(n+1)}+\beta^{(n+1)})$ and $\delta_2 = 1+2\hat{x}\alpha^{(n+1)} - \hat{y}\beta^{(n+1)} + (\hat{x}^2-\hat{y}^2)((\alpha^{(n+1)})^2 - (\beta^{(n+1)})^2)$.

Proof. The $(i,j)^{th}$ element of the matrix (3.1) can be written as

$$\hat{G}_{ji}^{(n+1)} = \bar{\hat{G}}_{ji}^{(n)} - \sum_{h,k} \bar{\hat{G}}_{jh}^{(n)}\left(\alpha^{(n+1)}W_{hk}^{(n+1)} + \beta^{(n+1)}P_{hk}^{(n+1)}\right)\hat{G}_{ki}^{(n+1)}. \tag{3.5}$$

From the definitions of $W_{ji}^{(n)}$ and $P_{ji}^{(n)}$ (see Lemma 2.1), since the block diagonal structure implies $\bar{\hat{G}}_{1h}^{(n)} = 0$ if $h > N_n$, we get

$$\begin{aligned}
\hat{G}_{11}^{(n+1)} &= \bar{\hat{G}}_{11}^{(n)} - \sum_{h,k} \bar{\hat{G}}_{1h}^{(n)}\left(\alpha^{(n+1)}W_{hk}^{(n+1)} + \beta^{(n+1)}P_{hk}^{(n+1)}\right)\hat{G}_{k1}^{(n+1)} \\
&= \bar{\hat{G}}_{11}^{(n)} - \left(\bar{\hat{G}}_{1b}^{(n)}\left(\alpha^{(n+1)}W_{bb}^{(n+1)}\hat{G}_{b1}^{(n+1)} + \beta^{(n+1)}P_{be}^{(n+1)}\hat{G}_{e1}^{(n+1)}\right)\right. \\
&\qquad \left. + \bar{\hat{G}}_{1d}^{(n)}\left(\alpha^{(n+1)}W_{dd}^{(n+1)}\hat{G}_{d1}^{(n+1)} + \beta^{(n+1)}P_{dr}^{(n+1)}\hat{G}_{r1}^{(n+1)}\right)\right) \\
&= \hat{G}_{11}^{(n)} - \left(\hat{G}_{1b}^{(n)}\left(\alpha^{(n+1)}\hat{G}_{b1}^{(n+1)} + \beta^{(n+1)}\hat{G}_{e1}^{(n+1)}\right)\right. \\
&\qquad \left. + \hat{G}_{1N}^{(n)}\left(\alpha^{(n+1)}\hat{G}_{b1}^{(n+1)} + \beta^{(n+1)}\hat{G}_{e1}^{(n+1)}\right)\right)
\end{aligned}$$

where $be, dr \in E_{\Omega_n}^{(1)}$ and in particular $b = (N_n+1)/2 = m_n$, $d = N_n$, $e = N_n+1$ and $r = 2N_n+1$. From symmetry $\left(\hat{G}_{b1}^{(n+1)} = \hat{G}_{d1}^{(n+1)},\ \hat{G}_{e1}^{(n+1)} = \hat{G}_{r1}^{(n+1)}\right)$, then

$$\hat{X} = \hat{x} - 2\hat{y}\left(\alpha^{(n+1)}\hat{G}_{b1}^{(n+1)} + \beta^{(n+1)}\hat{G}_{e1}^{(n+1)}\right). \tag{3.6}$$

Similarly,

$$\begin{aligned}
\hat{G}_{b1}^{(n+1)} &= \bar{\hat{G}}_{b1}^{(n)} - \sum_{h,k} \bar{\hat{G}}_{bh}^{(n)} \left(\alpha^{(n+1)} W_{hk}^{(n+1)} + \beta^{(n+1)} P_{hk}^{(n+1)}\right) \hat{G}_{k1}^{(n+1)} \\
&= \bar{\hat{G}}_{b1}^{(n)} - \left(\bar{\hat{G}}_{bb}^{(n)} \left(\alpha^{(n+1)} W_{bb}^{(n+1)} \hat{G}_{b1}^{(n+1)} + \beta^{(n+1)} P_{be}^{(n+1)} \hat{G}_{e1}^{(n+1)}\right)\right. \\
&\qquad \left. + \bar{\hat{G}}_{bd}^{(n)} \left(\alpha^{(n+1)} W_{dd}^{(n+1)} \hat{G}_{d1}^{(n+1)} + \beta^{(n+1)} P_{dr}^{(n+1)} \hat{G}_{r1}^{(n+1)}\right)\right) \\
&= \hat{G}_{m_n 1}^{(n)} - \left(\hat{G}_{m_n m_n}^{(n)} \left(\alpha^{(n+1)} \hat{G}_{b1}^{(n+1)} + \beta^{(n+1)} \hat{G}_{e1}^{(n+1)}\right)\right. \\
&\qquad \left. + \hat{G}_{m_n N_n}^{(n)} \left(\alpha^{(n+1)} \hat{G}_{b1}^{(n+1)} + \beta^{(n+1)} \hat{G}_{e1}^{(n+1)}\right)\right).
\end{aligned}$$

That is

$$\hat{G}_{b1}^{(n+1)} = \hat{y} - \left(\alpha^{(n+1)} \hat{G}_{b1}^{(n+1)} + \beta^{(n+1)} \hat{G}_{e1}^{(n+1)}\right) (\hat{x} + \hat{y}).$$

Hence,

$$\hat{G}_{b1}^{(n+1)} = \frac{\hat{y} - \beta^{(n+1)} \hat{G}_{e1}^{(n+1)} (\hat{x} + \hat{y})}{1 + \alpha^{(n+1)} (\hat{x} + \hat{y})}. \tag{3.7}$$

Also,

$$\begin{aligned}
\hat{G}_{e1}^{(n+1)} &= \bar{\hat{G}}_{e1}^{(n)} - \sum_{h,k} \bar{\hat{G}}_{eh}^{(n)} \left(\alpha^{(n+1)} W_{hk}^{(n+1)} + \beta^{(n+1)} P_{hk}^{(n+1)}\right) \hat{G}_{k1}^{(n+1)} \\
&= -\bar{\hat{G}}_{ee}^{(n)} \left(\alpha^{(n+1)} W_{ee}^{(n+1)} \hat{G}_{e1}^{(n+1)} + \beta^{(n+1)} P_{eb}^{(n+1)} \hat{G}_{b1}^{(n+1)}\right) \\
&\quad -\bar{\hat{G}}_{eq}^{(n)} \left(\alpha^{(n+1)} W_{qq}^{(n+1)} \hat{G}_{q1}^{(n+1)} + \beta^{(n+1)} P_{qz}^{(n+1)} \hat{G}_{z1}^{(n+1)}\right) \\
&= -\hat{G}_{11}^{(n)} \left(\alpha^{(n+1)} \hat{G}_{e1}^{(n+1)} + \beta^{(n+1)} \hat{G}_{b1}^{(n+1)}\right) \\
&\quad -\hat{G}_{1N}^{(n)} \left(\alpha^{(n+1)} \hat{G}_{q1}^{(n+1)} + \beta^{(n+1)} \hat{G}_{z1}^{(n+1)}\right),
\end{aligned}$$

where $q = 2N_n$ and $Z = 2N_n + m_n$. Since $\hat{G}_{q1}^{(n+1)} = \hat{G}_{z1}^{(n+1)}$,

$$\hat{G}_{e1}^{(n+1)} = -\hat{x}\alpha^{(n+1)} \hat{G}_{e1}^{(n+1)} - \hat{x}\beta^{(n+1)} \hat{G}_{b1}^{(n+1)} - \hat{y}\left(\alpha^{(n+1)} + \beta^{(n+1)}\right) \hat{G}_{q1}^{(n+1)}.$$

Hence,

$$\hat{G}_{e1}^{(n+1)} = \frac{-\hat{x}\beta^{(n+1)} \hat{G}_{b1}^{(n+1)} - \hat{y}\left(\alpha^{(n+1)} + \beta^{(n+1)}\right) \hat{G}_{q1}^{(n+1)}}{1 + \hat{x}\alpha^{(n+1)}}. \tag{3.8}$$

Finally,

$$\begin{aligned}\hat{G}_{q1}^{(n+1)} &= \bar{\hat{G}}_{q1}^{(n)} - \sum_{h,k} \bar{\hat{G}}_{qh}^{(n)} \left(\alpha^{(n+1)} W_{hk}^{(n+1)} + \beta^{(n+1)} P_{hk}^{(n+1)}\right) \hat{G}_{k1}^{(n+1)} \\ &= -\bar{\hat{G}}_{qe}^{(n)} \left(\alpha^{(n+1)} W_{ee}^{(n+1)} \hat{G}_{e1}^{(n+1)} + \beta^{(n+1)} P_{eb}^{(n+1)} \hat{G}_{b1}^{(n+1)}\right) \\ &\quad -\bar{\hat{G}}_{qq}^{(n)} \left(\alpha^{(n+1)} W_{qq}^{(n+1)} \hat{G}_{q1}^{(n+1)} + \beta^{(n+1)} P_{qz}^{(n+1)} \hat{G}_{z1}^{(n+1)}\right) \\ &= -\hat{G}_{N_n 1}^{(n)} \left(\alpha^{(n+1)} \hat{G}_{e1}^{(n+1)} + \beta^{(n+1)} \hat{G}_{b1}^{(n+1)}\right) \\ &\quad -\hat{G}_{N_n N_n}^{(n)} \left(\alpha^{(n+1)} \hat{G}_{q1}^{(n+1)} + \beta^{(n+1)} \hat{G}_{z1}^{(n+1)}\right).\end{aligned}$$

That is

$$\hat{G}_{q1}^{(n+1)} = -\hat{y}\left(\alpha^{(n+1)} \hat{G}_{e1}^{(n+1)} + \beta^{(n+1)} \hat{G}_{b1}^{(n+1)}\right) - \hat{x}\left(\alpha^{(n+1)} + \beta^{(n+1)}\right) \hat{G}_{q1}^{(n+1)}.$$

Hence,

$$\hat{G}_{q1}^{(n+1)} = \frac{-\hat{y}\left(\alpha^{(n+1)} \hat{G}_{e1}^{(n+1)} + \beta^{(n+1)} \hat{G}_{b1}^{(n+1)}\right)}{1 + \hat{x}\left(\alpha^{(n+1)} + \beta^{(n+1)}\right)}. \tag{3.9}$$

Equations (3.6)–(3.9) provide four equations in the four unknowns $\hat{X}, \hat{G}_{b1}^{(n+1)}, \hat{G}_{e1}^{(n+1)}$ and $\hat{G}_{q1}^{(n+1)}$. Rearranging these equations gives (using Mathematica) (Wolfram Research, Inc., 2014)

$$\hat{X} = \frac{3(\hat{x} - \hat{y})(\hat{x} + 2\hat{y}) + \Delta_1 + \Delta_2}{3(\hat{x} + \hat{y})}.$$

Also,

$$\hat{G}_{b1}^{(n+1)} = \frac{\hat{y}\left(1 + \alpha^{(n+1)}(\hat{x}^2 - \hat{y}^2)(\alpha^{(n+1)} + \beta^{(n+1)}) + \hat{x}(2\alpha^{(n+1)} + \beta^{(n+1)})\right)}{\delta_1 \delta_2}, \tag{3.10}$$

$$\hat{G}_{e1}^{(n+1)} = \frac{-\hat{y}\beta^{(n+1)}\left(\hat{x} + (\hat{x}^2 - \hat{y}^2)(\alpha^{(n+1)} + \beta^{(n+1)})\right)}{\delta_1 \delta_2} \tag{3.11}$$

and

$$\hat{G}_{q1}^{(n+1)} = \frac{-\hat{y}^2 \beta^{(n+1)}}{\delta_1 \delta_2}. \tag{3.12}$$

Now, for $\hat{Y} = \hat{G}_{s1}^{(n+1)}$, where $s = m_{n+1}$, (3.5) gives

$$\begin{aligned}
\hat{G}_{s1}^{(n+1)} &= \bar{\hat{G}}_{s1}^{(n)} - \sum_{h,k} \bar{\hat{G}}_{sh}^{(n)} \left(\alpha^{(n+1)} W_{hk}^{(n+1)} + \beta^{(n+1)} P_{hk}^{(n+1)}\right) \hat{G}_{k1}^{(n+1)} \\
&= -\bar{\hat{G}}_{se}^{(n)} \left(\alpha^{(n+1)} W_{ee}^{(n+1)} \hat{G}_{e1}^{(n+1)} + \beta^{(n+1)} P_{eb}^{(n+1)} \hat{G}_{b1}^{(n+1)}\right) \\
&\quad -\bar{\hat{G}}_{sq}^{(n)} \left(\alpha^{(n+1)} W_{qq}^{(n+1)} \hat{G}_{q1}^{(n+1)} + \beta^{(n+1)} P_{qz}^{(n+1)} \hat{G}_{z1}^{(n+1)}\right) \\
&= -\hat{G}_{m_n 1}^{(n)} \left(\alpha^{(n+1)} \hat{G}_{e1}^{(n+1)} + \beta^{(n+1)} \hat{G}_{b1}^{(n+1)}\right) \\
&\quad -\hat{G}_{m_n N_n}^{(n)} \left(\alpha^{(n+1)} \hat{G}_{q1}^{(n+1)} + \beta^{(n+1)} \hat{G}_{q1}^{(n+1)}\right)
\end{aligned}$$

since $\hat{G}_{z1}^{(n+1)} = \hat{G}_{q1}^{(n+1)}$, $\hat{G}_{se}^{(n)} = \hat{G}_{m_n 1}^{(n)}$ and $\hat{G}_{sq}^{(n)} = \hat{G}_{m_n N_n}^{(n)}$. Hence,

$$\hat{Y} = -\hat{y} \left(\alpha^{(n+1)} \hat{G}_{e1}^{(n+1)} + \beta^{(n+1)} \hat{G}_{b1}^{(n+1)}\right) - \hat{y} \left(\alpha^{(n+1)} + \beta^{(n+1)}\right) \hat{G}_{q1}^{(n+1)}. \tag{3.13}$$

Putting (3.10)–(3.12) into this equation gives

$$\hat{Y} = \frac{-\beta^{(n+1)} \hat{y}^2 \left(1 + (\hat{x} - \hat{y})(\alpha^{(n+1)} + \beta^{(n+1)})\right)}{\delta_1 \delta_2}.$$

□

The boundary conditions can now be considered via (3.2) to get (Algehyne & Mulholland, 2017),

$$\begin{aligned}
x &= \frac{\hat{x} + 2\hat{y}\bar{\gamma}_{m_n} y}{1 - \hat{x}\bar{\gamma}_1}, \\
y &= \frac{\hat{y}}{\left(1 - \hat{x}\bar{\gamma}_1\right)\left(1 - \bar{\gamma}_{m_n}(\hat{x} + \hat{y})\right) - 2\hat{y}^2 \bar{\gamma}_1 \bar{\gamma}_{m_n}}, \\
z &= \frac{\hat{x} + \hat{y}\bar{\gamma}_1 y + \hat{y}\bar{\gamma}_{m_n} r}{1 - \hat{x}\bar{\gamma}_{m_n}}
\end{aligned}$$

and

$$r = \frac{\hat{y}\left(1 + \bar{\gamma}_1 y \left(1 + \bar{\gamma}_{m_n}(\hat{y} - \hat{x})\right)\right)}{\left(\hat{x}\bar{\gamma}_{m_n} - 1 + \hat{y}\bar{\gamma}_{m_n}\right)\left(\hat{x}\bar{\gamma}_{m_n} - 1 - \hat{y}\bar{\gamma}_{m_n}\right)},$$

where $G_{11}^{(n)} = x$, $G_{1m_n}^{(n)} = y$, $G_{m_n m_n}^{(n)} = z$ and $G_{m_n N_n}^{(n)} = r$. The recursion relationships (3.3) and (3.4) require initial values for $\hat{x}$ and $\hat{y}$. To obtain these the matrix, $\hat{A}^{(1)}$ is formed from (1.12) where $H^{(1)}$ is given by inserting $n = 1$ into (2.5)–(2.7), and $K^{(1)}$ from (2.12)–(2.14). It transpires that $\hat{A}_{ii}^{(1)} = 36 + q^2$ where $i = 1, 2, 3$ and $\hat{A}_{ji}^{(1)} = 2 + (q^2/6)$ where $j, i = 1, 2, 3$ and $j \neq i$. Hence, $\hat{x} = \hat{G}_{11}^{(1)} = ((\hat{A}^{(1)})^{-1})_{11}$

and $\hat{y} = \hat{G}_{12}^{(1)} = ((\hat{A}^{(1)})^{-1})_{12}$. From Algehyne & Mulholland (2017), the non-dimensionalized electrical impedance is then given by

$$\hat{Z}_E(f;n) = \frac{Z_T}{C_0 q c_{44}^T \xi Z_0}\left(1 + \frac{\zeta^2 C_0 \eta}{c_{44}^T \xi}(\sigma_1 + \sigma_2)\right), \tag{3.14}$$

where $C_0 = A_r \varepsilon_{11}/L$ is the transducer capacitance, Z_0 is the series electrical impedance load in the connecting circuitry, $\sigma_1 = \gamma_1\left(G_{1m_n}^{(n)} - G_{11}^{(n)}\right)$ and $\sigma_2 = \gamma_{m_n}\left(-G_{m_nN_n}^{(n)} - G_{m_nm_n}^{(n)} + 2G_{1m_n}^{(n)}\right)$. The non-dimensionalized transmission sensitivity ψ is then given by (Algehyne & Mulholland, 2017)

$$\psi(f;n) = \frac{aZ_L}{\left(Z_E + b\right) c_{44}^T \xi C_0} K^{(n)}, \tag{3.15}$$

where $a = Z_P/(Z_0 + Z_P)$, $b = Z_0 Z_P/(Z_0 + Z_P)$, Z_P is parallel electrical impedance load and $K^{(n)} = \gamma_{m_n}\left(-\eta\left(\gamma_1 G_{1m_n}^{(n)} - \gamma_{m_n}\left(G_{m_nm_n}^{(n)} + G_{m_nN_n}^{(n)}\right)\right) + 1\right)$. The non-dimensionalized reception sensitivity ϕ is then (Algehyne & Mulholland, 2017)

$$\phi(f;n) = \frac{2\zeta e_{24} L \eta \sigma_2}{\xi c_{44}^T}\left(1 - \frac{aZ_T \zeta^2 \eta\left(\sigma_1 + \sigma_2\right)}{\left(Z_E + b\right) q\left(c_{44}^T\right)^2 \xi^2} - \frac{aZ_T}{\left(Z_E + b\right) q c_{44}^T \xi C_0}\right)^{-1}. \tag{3.16}$$

4. Results

As a result of the equations presented above, a comparison between the key operating characteristics of the transmission and reception spectra of the fractal and standard (Euclidean) designs (Hayward, 1984) can now be evaluated and compared. The key parameters of interest to be compared between both models include the amplitude (or gain) and the bandwidth (the range of frequencies over which a certain gain, expressed in decibels, is exceeded). To evaluate the transmission and reception sensitivities of the fractal device, the fractal generation levels were gradually increased and the differences in these parameters observed. However, with the aim of physically producing the device, we will focus on the fractal generation level $n = 3$. From a practical perspective, these fractal transducers will only be able to be manufactured at low fractal generation levels. To perform a fair comparison, the volume of piezoelectric material in the standard design (vol_E) and fractal design (vol_F) is kept consistent. The volume of the piezoelectric material in the standard design is $vol_E = L^2 d_E = LA_E$, where L is the length of the front face, d_E is the thickness and A_E is the area occupied by the electrode. The volume of the piezoelectric material in the fractal design is $vol_F = S_n d_F$, where S_n is the area of the front face of the fractal piezoelectric design at generation level n (the black area in Fig. 6) and d_F is the thickness; the area S_n is then given by $S_n = \sqrt{3}L^2\left(1 - (3/4)^{n+1}\right)/4$ and equating vol_E and vol_F gives $d_F = L^2 d_E/S_n$. The fractal transducer has one electrode of area $A_F' = d_F h^{(n)}/2$ at one face and two electrodes of area A_F' each on the opposite face (see Fig. 6). As the device operates essentially as a capacitor in this circuit, and since the total capacitance of two capacitors in parallel is just the sum of those two capacitances, then we take the total area to be $A_F = 2A_F' = d_F h^{(n)} = d_F L/2^n$. By choosing a particular value for the fractal generation level n, the thickness d_E and the length L, this sets d_F, which in turn sets A_E, A_F and the volume of piezoelectric material. The behaviour of the device is dictated by its electrical

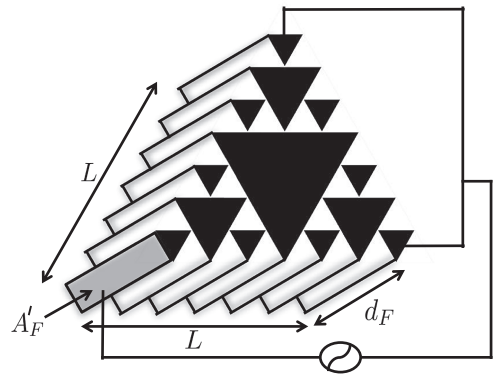

FIG. 6. A three-dimensional schematic of the Sierpinski gasket ultrasonic transducer at fractal generation level $n = 2$. The black triangles are the front faces of the piezoelectric material. The device is connected to an electrical circuit as shown where each electrode has surface area A'_F.

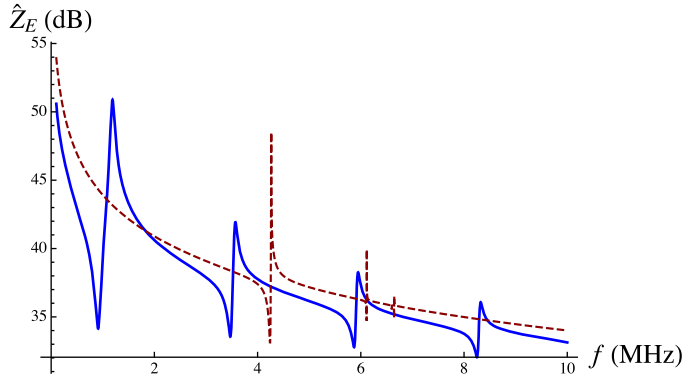

FIG. 7. Non-dimensionalized electrical impedance (equation (3.14)) versus frequency for the $\overline{\text{SG}}$ transducer at fractal generation level $n = 3$ (dashed line). The non-dimensionalized electrical impedance of the standard (Euclidean) transducer (Hayward, 1984) is plotted for comparison (full line). Parameter values are given in Table 1.

resonances, which in turn depend on its capacitance. The capacitance depends on the distance between the electrodes, which remains fixed in the conventional design. So, to assist in the comparison between the standard design and the fractal design, the distance between the electrodes was held fixed in the fractal case too. A different scenario could be studied where the surface area remains fixed and the edge length L is varied. To enable a frequency domain analysis, we set $q \to \sigma + j\omega$ where $\sigma, \omega \in \mathbb{R}$, σ is a damping term (set to zero in this paper), ω is the angular frequency and j is the square root of -1.

The characteristic profile of the electrical impedance spectrum (magnitude) for both models where $n = 3$ is illustrated in Fig. 7. The fractal design, given by (3.14), is represented by the dashed line while the equivalent standard design is represented by the full line (Hayward, 1984). It can be seen that the behaviour is predominantly that of a capacitor it decreases according to a $1/(C_0 f)$ profile where C_0 is the capacitance and f is the frequency with a few resonant peaks superimposed on this. From the above analysis, $A_E = \sqrt{3}\,(1 - (3/4)^{n+1})\,2^{(n-3)} A_F$ and the coefficient of A_F is monotonically increasing as a function of the fractal generation level n and is greater than one for all $n \geqslant 3$. Hence,

TABLE 1 *Parameter values for the front and back mechanical loads and the electrical load (Mulholland et al., 2007; Mulholland & Walker, 2011)*

Design parameter	Symbol	Magnitude	Dimensions
Parallel electrical impedance load	Z_P	1000	Ohms
Series electrical impedance load	Z_0	50	Ohms
Length of SG	L	1	mm
Mechanical impedance of the front load	Z_L	1.5	MRayls
Mechanical impedance of the backing layer	Z_B	2	MRayls
Wave speed in the front load	c_L	1500	ms^{-1}
Wave speed in the backing layer	c_B	1666	ms^{-1}
Density of the front load	ρ_L	1000	kgm^{-3}
Shear modulus of the front load	μ_L	2.25×10^9	Nm^{-2}
Shear modulus of the backing layer	Y_B	2.78×10^9	Nm^{-2}
Thickness of the piezoelectric material in the standard (Euclidean) design	d_E	10	mm

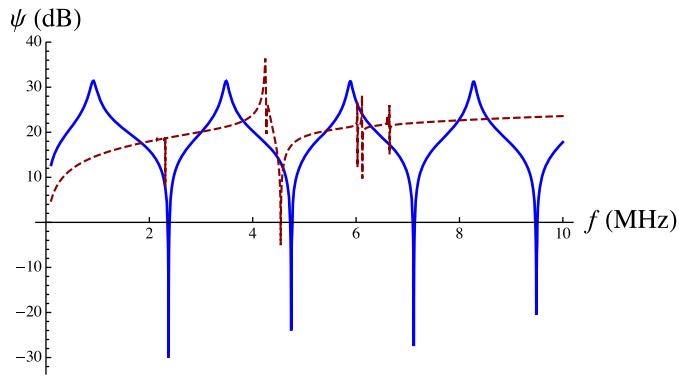

FIG. 8. Non-dimensionalized transmission sensitivity (equation (3.15)) versus frequency for the $\overline{\text{SG}}$ transducer at fractal generation level $n = 3$ (dashed line). The non-dimensionalized transmission sensitivity of the standard (Euclidean) transducer (Hayward, 1984) is plotted for comparison (full line). Parameter values are given in Table 1.

for reasonable values of n, $A_E \gg A_F$. Since $C_0 = A_{E/F}\,\varepsilon_{11}/L$, then $C_{0_E} \gg C_{0_F}$ (where $C_{0_{E/F}}$ is the capacitance in the E-standard / F-fractal design) and so $1/(C_{0_E} f) \ll 1/(C_{0_F} f)$. Since the standard design has a larger capacitance, then this explains why its electrical impedance is in general lower. The locations and magnitudes of the first maximum (f_a) and first minimum (f_r) turning points are the critical features for a design engineer. In transmission mode, the device should be driven at the mechanical resonance frequency (the frequency at the first minimum) where it will deliver the maximum force on the load. In reception mode however, the device should be driven at the frequency of the first maximum (the electrical resonance frequency). As shown in Fig. 7, for the standard design (full line) $f_r = 0.9$ MHz, $|\hat{Z}_E(f_r)| = 34$ dB, $f_a = 1.2$ MHz and $|\hat{Z}_E(f_a)| = 51$ dB. As discussed above, these frequencies correspond precisely to the first maximum in the transmission sensitivity plot (Fig. 8; full line) and the reception sensitivity plot (Fig. 9; full line).

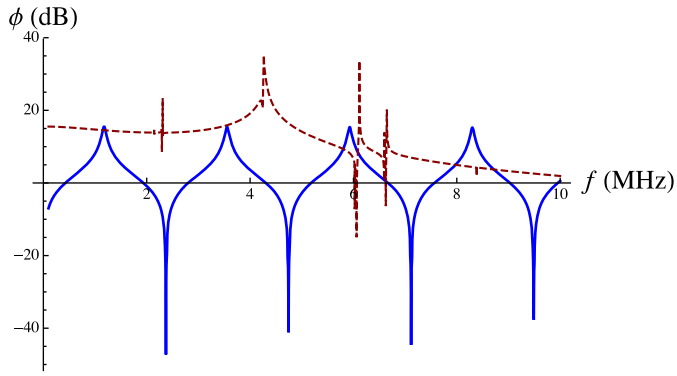

FIG. 9. Non-dimensionalized reception sensitivity (equation (3.16)) versus frequency for the $\overline{\text{SG}}$ transducer at fractal generation level $n = 3$ (dashed line). The non-dimensionalized reception sensitivity of the standard (Euclidean) transducer (Hayward (1984)) is plotted for comparison (full line). Parameter values are given in Table 1.

TABLE 2 *A comparison between the operating characteristics of a fractal transducer and an equivalent standard design at fractal generation level $n = 3$. The mechanical resonance frequency is denoted by f_r (MHz), the electrical resonance frequency is denoted by f_a (MHz), the transmission sensitivity gain is denoted by ψ_{max} (dB), the reception sensitivity gain is denoted by ϕ_{max} (dB), the transmission sensitivity bandwidth is denoted by BW_T (MHz) and the reception sensitivity bandwidth is denoted by BW_R (MHz)*

Design	f_r (MHz)	f_a (MHz)	ψ_{max} (dB)	ϕ_{max} (dB)	BW_T (MHz)	BW_R (MHz)
Fractal	4.2	4.3	37.0	35.0	0.1	3.2
Standard	0.9	1.2	32.0	17.0	0.2	0.2

The piezoelectrically stiffened velocity (c_T) in (1.7), calculated from the parameter values for PZT-5H (see Auld, 1973), is 2370 min/s giving an electrical resonance frequency $f_a = c_T/(2L) = 1.2$ MHz for a device of length $L = 1$ mm. This agrees reasonably well with the reception sensitivity maximum for the homogenized estimate for f_a (the full line in Fig. 9). The fractal device produces an electrical impedance spectrum that has a richer set of resonances and this is due to the many length scales inherent to its structure. To show all of the resonances, the zero damping case is shown ($\sigma = 0$); when even a small level of damping is added, the resonances that have a very narrow support (such as those at frequencies 2.2 MHz and around 6 MHz) do not appear in these plots. Note however that the electrical impedance gain of the fractal design is lower than the standard design by around 2 dB at the optimal reception frequency ($f_r^{(3)} = 4.2$ MHz, $|\hat{Z}_E(f_r; 3)| = 33$ dB, $f_a^{(3)} = 4.3$ MHz and $|\hat{Z}_E(f_a; 3)| = 49$ dB). Figure 8 shows that the transmission sensitivity of the fractal design has a maximum amplitude (gain) that is higher than the Euclidean case (standard design) at its lower operating frequency (37 dB at 4.2 MHz compared to 32 dB at 3.5 MHz for the Euclidean case). However, the bandwidth is reduced; at 3 dB below the maximum amplitude of the standard design, i.e. 29 dB, the bandwidth of the fractal design is 0.1 MHz and the standard design is 0.2 MHz. Figure 9 shows that the reception sensitivity spectrum has a much larger gain; there is an 18 dB improvement in the reception sensitivity gain from the standard design to the fractal design. This peak in the reception sensitivity also results in an enhanced bandwidth; if we take the noise floor to be 3 dB below the peak gain of the standard design (i.e. the 14 dB level

in this plot), then the operational bandwidth of the standard design is 0.2 MHz, whereas the fractal design has an operational bandwidth of around 3.2 MHz (a summary of these comparisons is provided in Table 2).

5. Summary and conclusion

Using a design based on fractal geometry, a theoretical model of a piezoelectric ultrasound transducer was produced and analysed in this paper. This showed that the fractal design has certain advantages over the current technology. The critical innovation was to base the design on the complement of the Sierpinski gasket as this introduces a range of length scales within the resonating structure. Using a finite element methodology, the weighted graph counterpart of this fractal (denoted $\overline{\mathrm{SG}}$) was used to support the electrical and mechanical fields. New basis functions were derived; however, since this is the first finite element analysis on this graph. These are resonating devices and since the standard design typically has a single length scale, while the fractal design has multiple length scales, it is unsurprising that this results in a much richer set of resonance frequencies; it is well known in fact that musical instruments and naturally occurring auditory systems rely precisely on this very principle. The finite element formulation discretized the problem to produce a matrix equation and, benefitting from its block diagonal structure, the inversion of this matrix was achieved using a renormalization approach. The symmetry of the structure is embedded in these renormalization equations and this enabled us to describe the dynamics of the structure via only two coupled recursion relationships. These pivotal Green's functions were then used in expressions for the transmission and reception sensitivities of the device. From a practical perspective, it will only be possible to manufacture these devices for a small number of fractal generation levels. Hence, the results produced in this paper focus on low-generation levels (pre-fractals) but it is worth emphasizing that the dynamics of the true fractal can also be examined by studying the steady states of the recursion relationships. As anticipated, the model predicts that, in comparison to the standard transducer, this pre-fractal transducer has more resonance frequencies. In addition, the fractal transducer also produced a higher amplitude (or gain) in transmission and reception sensitivities than the standard design, a 5 dB increase in transmission mode and an 18 dB increase in reception mode. The reception sensitivity also resulted in a wider bandwidth than the standard design, a 3 MHz increase. The encouraging theoretical results in this paper have led to a manufacturing programme of work. A piezoelectric ultrasonic transducer has been successfully manufactured whose design is the complement of the Sierpinski gasket; full details can be found in the paper by Fang *et al.* (2018). The manufacturing process involved a combination of 3D printing and a piezoelectric pillar placement methodology. As was done here in this theoretical paper, two equivalent (same volume of piezoelectric material) 1-3 piezocomposite designs were manufactured and experimentally compared, one with a standard design and one with the fractal geometry. It was found that there was a marked improvement in both bandwidth and sensitivity when using the fractal device. The fractal device was also experimentally compared to a commercial transducer and over a 100% bandwidth improvement was found.

Funding

The authors gratefully acknowledge the support given by the University of Tabuk, Ministry of Education in Saudi Arabia and the Royal Embassy of Saudi Arabia in UK. United Kingdom Engineering and Physical Sciences Research Council (EP/P005268/1).

References

Abdulbake, J., Mulholland, A. J. & Gomatam, J. (2003) A renormalization approach to reaction–diffusion processes on fractals. *Fractals*, **11**, 315–330.

Abdulbake, J., Mulholland, A. J. & Gomatam, J. (2004) Existence and stability of reaction–diffusion waves on a fractal lattice. *Chaos Solitons Fractals*, **20**, 799–814.

Algehyne, E. A. & Mulholland, A. J. (2015a) A finite element approach to modelling fractal ultrasonic transducers. *IMA J. Appl. Math.*, **80**, 1684–1702.

Algehyne, E. A. & Mulholland, A. J. (2015b) Sensor mimics nature to detect dangerous structural cracks. *Homeland Defense and Security Information Analysis Center (HDIAC) Spotlight*. Available at https://www.hdiac.org/node/2163.

Algehyne, E. A. & Mulholland, A. J. (2017) Renormalization analysis of a composite ultrasonic transducer with a fractal architecture. *Fractals*, **25**, 1750015.

Alippi, A., Bettucci, A., Craciun, F., Farrelly, F., Molinari, E. & Petri, A. (1993) Acoustic modes in 2-dimensional self-similar composite plates. *1993 Proceedings IEEE Ultrasonics Symposium*, IEEE: Baltimore, MA, USA, pp. 533–536, vol. 1. doi: 10.1109/ULTSYM.1993.339553.

Auld, B. A. (1973) *Acoustic Fields and Waves in Solids*, vol. 1. New York: John Wiley and Sons.

Barlow, E., Algehyne, E. A. & Mulholland, A. J. (2016) Investigating the performance of a fractal ultrasonic transducer under varying system conditions. *Symmetry*, **8**, 43–72.

Barlow, M. T. (1998) Diffusion on fractals. *Lectures on Probability Theory and Statistics* (P. Bernard ed.). Lecture Notes in Mathematics, vol. 1690. Berlin: Springer, pp. 1–121.

Beyer, R. T. & Letcher, S. V. (1969) *Physical Ultrasonics*. New York: Academic Press.

Chiselev, A. M., Moraru, L. & Gogu, A. (2009) Localization of an object using a bat model inspired from biology. *J. Biophys.*, **19**, 251–258.

Derfel, G., Grabner, P. J. & Vogl, F. (2012) Laplace operators on fractals and related functional equations. *J. Phys. A*, **45**, 463001.

Eberl, D. F., Hardy, R. W. & Kernan, M. J. (2000) Genetically similar transduction mechanisms for touch and hearing in *Drosophila*. *J. Neurosci.*, **20**, 5981–5988.

de Espinosa, F. M., Martinez, O., Elvira Segura, L. & Gómez-Ullate, L. (2005) Double frequency piezoelectric transducer design for harmonic imaging purposes in NDT. *IEEE Trans. Ultrason. Ferroelectr. Freq. Control*, **52**, 980–986.

Falconer, K. J. & Hu, J. (2001) Nonlinear diffusion equations on unbounded fractal domains. *J. Math. Anal. Appl.*, **256**, 606–624.

Fang, H., Qiu, Z., Mulholland, A., O'Leary, R. & Gachagan, A. (2018) Broadband 1-3 piezoelectric composite transducer design using Sierpinski gasket fractal geometry. *IEEE IEEE Trans. Ultrason. Ferroelectr. Freq. Control*, **65**, 2429–2439. doi: 10.1109/TUFFC.2018.2874384

Giona, M. (1996) Transport phenomena in fractal and heterogeneous media—input/output renormalization and exact results. *Chaos Solitons Fractals*, **7**, 1371–1396.

Giona, M., Schwalm, W. A., Schwalm, M. K. & Adrover, A. (1996) Exact solution of linear transport equations in fractal media—I. Renormalization analysis and general theory. *Chem. Eng. Sci*, **51**, 4717–4729.

Hayward, G. (1984) A systems feedback representation of piezoelectric transducer operational impedance. *Ultrasonics*, **22**, 153–162.

iRAP (2016) Piezoelectric sensors and ultrasonic transducers—types, materials, applications, new developments, industry structure and global markets. *Technical Report ET-127*. Available at http://www.innoresearch.net.

Kigami, J. (2001) *Analysis on Fractals*. Cambridge, UK: Cambridge University Press.

Miles, R. N. & Hoy, R. R. (2006) The development of a biologically-inspired directional microphone for hearing aids. *Audiol. Neurootol.*, **11**, 86–94.

Mulholland, A. J. (2008) Bounds on the Hausdorff dimension of a renormalisation map arising from an excitable reaction–diffusion system on a fractal lattice. *Chaos Solitons Fractals*, **35**, 274–284.

Mulholland, A. J., Ramadas, S. N., O'Leary, R. L., Parr, A. S., Troge, A., Hayward, G. & Pethrick, R. A.

(2007) A theoretical analysis of a piezoelectric ultrasound device with an active matching layer. *Ultrasonics*, **47**, 102–110.

Mulholland, A. J. & Walker, A. J. (2011) Piezoelectric ultrasonic transducers with fractal geometry. *Fractals*, **19**, 469–479.

Mulholland, A. J., Walker, A. J., Mackersie, J. W., O'Leary, R. L., Gachagan, A. & Ramadas, N. (2011) The use of fractal geometry in the design of piezoelectric ultrasonic transducers. *Ultrasonics Symposium (IUS), 2011 IEEE International.* IEEE: Orlando, FL, pp. 1559–1562. doi: 10.1109/ULTSYM.2011.0387.

Müller, R. (2004) A numerical study of the role of the tragus in the big brown bat. *J. Acoust. Soc. Am.*, **116**, 3701–3712.

Müller, R., Lu, H., Zhang, S. & Peremans, H. (2006) A helical biosonar scanning pattern in the Chinese noctule Nyctalus plancyi. *J. Acoust. Soc. Am.*, **119**, 4083–4092.

Nadrowski, B., Albert, J. T. & Göpfert, M. C. (2008) Transducer-based force generation explains active process in *Drosophila* hearing. *Curr. Biol.*, **18**, 1365–1372.

Orr, L. A., Mulholland, A. J., O'Leary, R. L. & Hayward, G. (2008) Analysis of ultrasonic transducers with fractal architecture. *Fractals*, **16**, 333–349.

Orr, L. A., Mulholland, A. J., O'Leary, R. L., Parr, A., Pethrick, R. & Hayward, G. (2007) Theoretical modelling of frequency dependent elastic loss in composite piezoelectric transducers. *Ultrasonics*, **47**, 130–137.

Robert, D. & Göpfert, M. C. (2002) Novel schemes for hearing and orientation in insects. *Curr. Opin. Neurobiol.*, **12**, 715–720.

Schwalm, W. A. & Schwalm, M. K. (1988) Extension theory for lattice Green functions. *Phys. Rev. B Condens. Matter*, **37**, 9524–9542.

Strichartz, R. S. (1999) Analysis on Fractals. *Notices Amer. Math. Soc.*, **46**, 1199–1208.

Wolfram Research, Inc. (2014) Mathematica. Version 10.0. Champaign, Illinois.

Yang, J. (2006a) *Analysis of Piezoelectric Devices*. Singapore: World Scientific.

Yang, J. (2006b) *The Mechanics of Piezoelectric Structures*. Singapore: World Scientific.